

Development of a Damped Piezoresistive MEMS High Shock Sensor

Robert D. Sill
PCB Piezotronics Inc.
951 Calle Negocio, Suite A
San Clemente, CA 92673
rsill@pcb.com (949) 429 5259 x23

Abstract

Piezoresistive (PR) silicon accelerometers with micro-electromechanical systems (MEMS) technology are preferred in many high shock impact measurements. These devices exploit the strength of single crystal silicon (SCS) along with the minimal zero shifting associated with PR sensors. However, an undesirable characteristic of SCS is its extremely low internal damping, which results in susceptibility to overshoot and resonant excitation. The most commonly used MEMS devices for extreme shock applications were designed to maximize their resonant frequency. The intent was to avoid accelerometer over range problems by locating the resonance of the accelerometer above the frequency content of any mechanical excitation stimuli. However, surprisingly low energy impacts were still found to cause resonance amplification and resultant failure. More energetic impacts easily exceeded the capabilities of this older design. As a byproduct of these megahertz resonances, resultant sensor seismic element displacements were so small that effectively no internal damping was possible. Because of this lack of damping, bulky external mechanical isolators have to be frequently employed to protect the transducer (isolate it from high frequencies). Isolator design has to pay considerable attention to preserving enough bandwidth to track the residual rigid body motion and/or structural dynamics of interest for the device under test. A different approach in MEMS shock sensor design is described in this paper. In this approach, the resonance frequency is intentionally lowered to reduce the response of the accelerometer to higher frequency energy that may be present in shock events. The relatively low resonance enables displacements of the seismic element sufficient to introduce squeeze film damping using air as the medium. Air is used since thermal effects on its performance are negligible. The design is manufactured using recent advances in semiconductor processing, and aims at a mildly under damped sensor with sufficient bandwidth to accurately measure test item rigid-body or structural response over the frequency range of interest. Accelerometer resonant amplification is reduced by orders of magnitude, and accelerometer survivability is increased.

Introduction

Accelerometers used in high shock environments, particularly in the measurement of the penetration of earth and concrete and pyrotechnic type environments, are typically based on undamped piezoresistive (PR) micro-electromechanical systems (MEMS) sensors. Such PR devices are chosen due to the strength of single crystal silicon and the superiority of their zero shift characteristics over other transduction mechanisms, such as piezoelectric sensors.

The most common commercial PR device presently used in the high shock environments was designed with the intent to maximize resonance frequency. It was expected that achieving resonance on the order of 10^6 Hz was adequate to assure survivability. However the rise times of many energetic impacts proved to be so short, and the resonant amplification of the undamped device was so high, that failures of this traditional device due to overshoot and “ringing” became common. Although that design became the

standard for measurements in extreme environments, the ongoing trend in structural systems' design appears to be for increasingly higher energy levels, so a new approach is necessary.

In the past these failures motivated the development of mechanical isolators which severely reduced the frequency content experienced by the transducer [1]. In most applications this reduction of bandwidth was adequate, even preferred over the wideband signal, such as in the measurement of rigid body deceleration of vehicles. It was desired, however, to avoid the need for the mechanical isolator, and attempt to design the filtration into the sensors.

Description

The MEMS device described in this paper was intentionally designed with a relatively low resonant frequency. This provides natural filtering, that is, attenuation of frequency components above the resonance, and also allows sufficient displacement of the inertial seismic mass so that it is possible to incorporate squeeze film damping. The intent of the damping is to reduce the extremely high resonant amplification inherent in single crystal silicon. Since the "Q" of silicon structures can be above 1000, even attaining only a few percent of critical damping cuts that amplification by two orders of magnitude. (Since $Q = 1/(2\zeta)$, if the critical damping ratio ζ has a value of 0.05, Q would be 10.) Also, since the mechanism of squeeze film damping necessarily includes structures close to the inertial mass, protective stops therefore become available. Survivability is expected to be enhanced by the prevention of over travel and the reduction of overshoot and resonant amplification.

The other primary difference in the new sensor is the resistance of the bridge, which is approximately 5000 Ohms, almost ten times higher than the traditional design. The lifespan of battery powered applications using this sensor would be significantly increased.

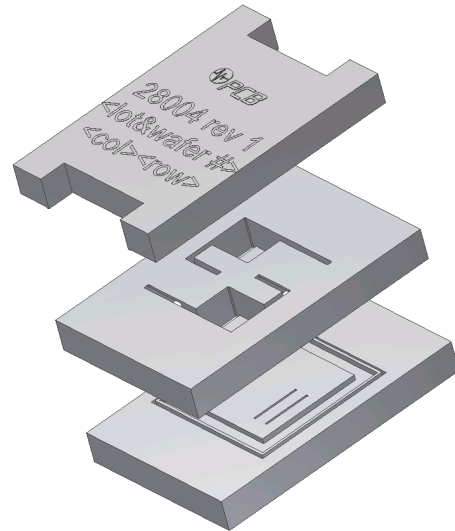
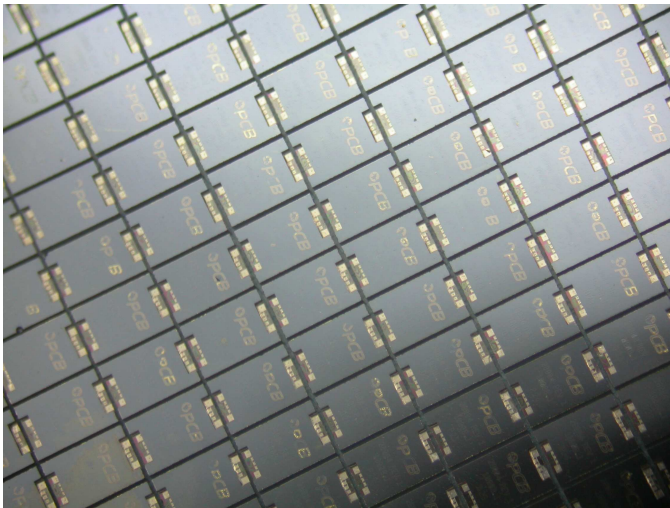


Figure 1. Array of MEMS sensors, left, and the layers in an individual sensor, right.

The photograph in Figure 1 shows the spacing and the saw cuts to singulate the sensors from the stacked assembly of three wafers. The identification is seen on top of the Lid wafer, and aluminum wirebond pads on the Core wafer are seen through an access hole in the Lid. (Details of the Core are shown in a photograph in Figure 2.) Beneath the Core is the Base layer, which forms a stop to prevent overtravel of the inertial mass downward during positive accelerations, just as the Lid provides protection during upward motion from negative accelerations. In both the Lid and Base stop region are grooves to control the damping of the squeeze film of trapped air. Glass frit is applied in the area around the central region to hold the layers together, as well as to provide a hermetic seal.

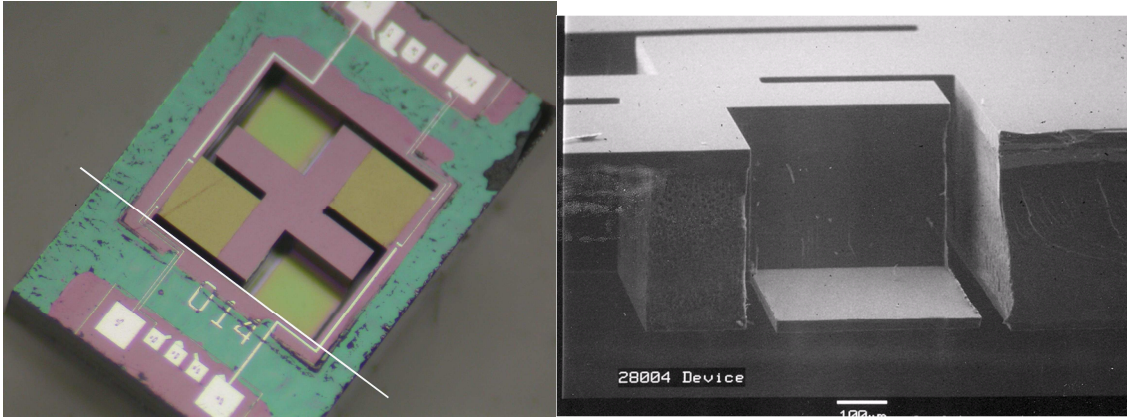


Figure 2. Core layer of sensor with Lid removed, left, and Scanning Electron Microscopy, right. The white line drawn in the photograph is approximately the plane of the break in the Core wafer which allowed the viewing angle of the SEM image.

The glass frit used to bond the Base to the Core and the Core to the Lid is the teal-colored residue around the periphery of central area shown in Figure 2. The purple oxide-covered silicon is seen in the wirebond pad areas as well as the cross-shaped mass. Gold-colored thinner oxide covers the ion-implanted strain gauge resistors on the cantilevers. The four larger aluminum pads are the wirebond pads.

Key to the performance of this sensor is the precise control of the geometries of the Core layer through recent advances in semiconductor processing, visible in the SEM of Figure 2. It is the uniformity and symmetry between these components from which the performance advantages come with this MEMS design, such as amplitude linearity and transverse sensitivity. The contrast between geometry and manufacturing techniques used in various PR MEMS devices is shown in Figure 3.

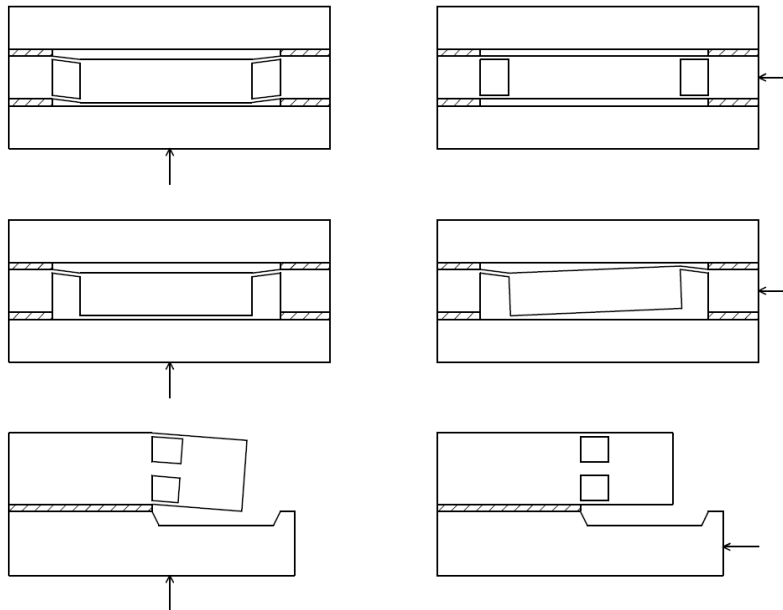


Figure 3. PR MEMS configurations in cross section, showing deflections due to normal and transverse accelerations.

The sketches on the upper row of Figure 3 depict the sensor configuration in this paper, including the thin flexure elements symmetrically above and below the center of mass of the inertial element. The asymmetric configuration in the middle row shows the rotation of the mass expected in transverse acceleration when

the flexures are only on one surface of the mass. The bottom row depicts the rotation of the inertial mass in the design of the traditional high shock PR sensor.



Figure 4. Packaging of the 3991F3JB20.

Since many fixtures in the shock community are based on the traditional sensor package, the new sensor package shown in Figure 4 has compatible dimensions. However, the package shown is substantially different from the traditional stainless steel package and its cable made of copper conductors. The new housing is titanium, therefore lighter, and the cable is stronger, made of silver coated Kevlar. To avoid noise observed in the traditional cable, triboelectric noise treatment is included in the cable shown.

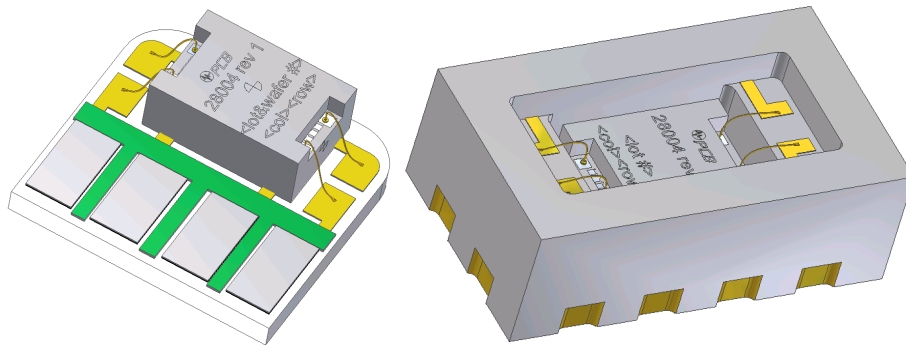


Figure 5. The subassembly of the 3991F3JB20, left, and a surface mount package, right.

Inside the housing of Figure 4 is the subassembly depicted at the left of Figure 5, consisting of the sensor epoxied to an alumina substrate and connected with wirebonds. That subassembly is an accelerometer in its own right, capable of being installed on circuit boards or housings. The ceramic package depicted at the right (shown open for clarity, but which would be covered and sealed) is designed for surface mount applications.

Performance

Capabilities of the new sensor is still in the process of evaluation. Initial tests show that performance generally matched predictions. Sensitivity of the latest batch averaged 0.0096 mV/G with 10 V excitation, resonant frequency was 68kHz, with damping coefficient of approximately 5%.

Samples from the latest (second) batch of sensors are being distributed to facilities for testing in the field. One such test on the first batch is shown in Figure 5, of a sequence of Hopkinson bar tests side by side with the traditional sensor. This early prototype had stop level set above 80kG, and as a consequence had damping somewhat smaller than desired. The results should be considered an indicator of damping that is lower than expected in the second and later batches.

The test in Figure 6a was at ~40000 G, 6b ~80000 G and 6c ~120000 G. In the first two tests, the two traces of the side-by-side transducers were well correlated for the initial pulse. Both devices had the same excitation voltage and gain. The traces show the larger sensitivity of the 3991 during the primary pulse

(nominally 10 $\mu\text{V}/\text{G}$ (20000 G full scale) vs 3 $\mu\text{V}/\text{G}$ for the 60000 G full scale of the other transducer). In the third test the protective stops of the new sensor engaged. Note the ringing of the undamped transducer increased from one half the primary pulse in **a** to twice the initial amplitude in **c**, whereas the damping of the 3991 kept its ringing well below the amplitude of the primary pulse, despite the discontinuity of hitting the stops in **c**.

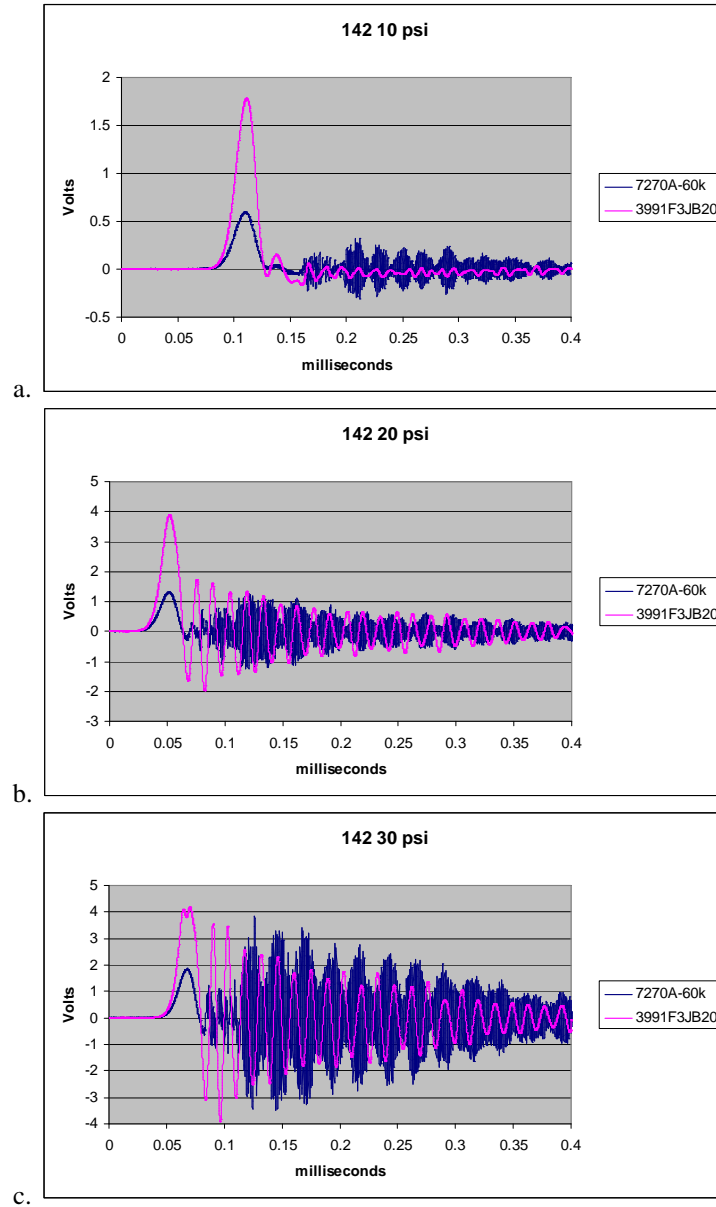


Figure 6. Hopkinson Bar tests on a flyaway, side by side with an undamped transducer. Data is courtesy of Eglin AFB AFRL.

Results of sensitivity and amplitude linearity is shown in Figures 7 and 8, as tested with the pneumatic shock equipment described in reference [2] and pictured in Figure 9.

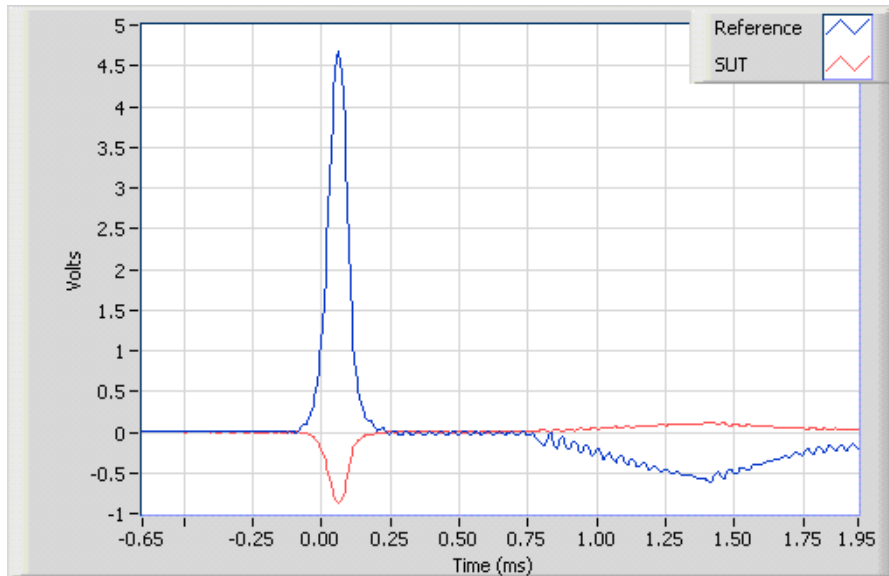


Figure 7. Comparison shock testing to 10000 G. The blue trace is that of the back-to-back reference transducer, and the red trace is the sensor under test. Sensitivity is calculated by comparing the peak values.

The time domain plot in Figure 7 shows an unusual test in which the package is upside down. (This configuration is not recommended in the field because the weldment on the top is insufficiently flat to be a good mounting surface). The resulting sensitivity is one of many tests plotted to evaluate the amplitude linearity in Figure 8.

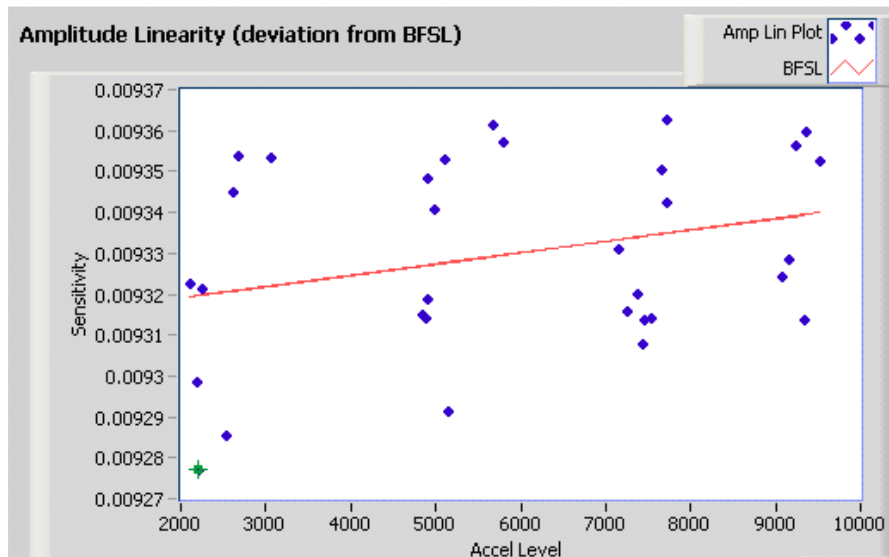


Figure 8. Amplitude linearity is calculated as the Best Fit Straight Line of sensitivity as a function of acceleration.

The plot in Figure 8 summarizes 32 tests on one sensor between 2000 G and 10000 G. The average value was 0.00933 mV/G with 10V excitation. The slope of the line indicates that sensitivity increases by 0.28% per 10000 G for this particular sensor. Maximum deviation from the Best Fit Straight Line is less than 0.5%. It was observed that some of the scatter was due to the inverted mounting, however, it did not affect the slope.

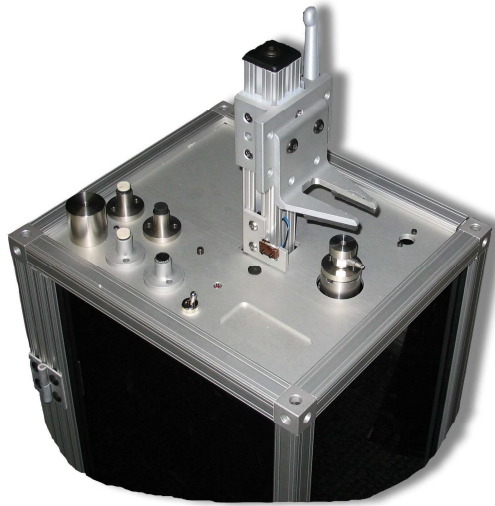


Figure 9. Pneumatic shock test apparatus. This device was used to take the amplitude linearity data shown in Figure 7. It was described in reference [2], and provides shocks from below 100 G to 10000 G for comparison calibrations tests. Tests through the full scale range and through to the levels at which the stops were engaged were performed on a Hopkinson bar.

In the second lot of accelerometers, Hopkinson bar testing was used to evaluate amplitude linearity through and beyond the linear range, until stops were engaged, as shown in Figure 10. In this lot, the level of stops was approximately 40000 G. The results in tests below the stops showed little nonlinearity, although the repeatability and uncertainty of Hopkinson bar tests are considerably greater than that of the technique shown in Figures 7 and 9.

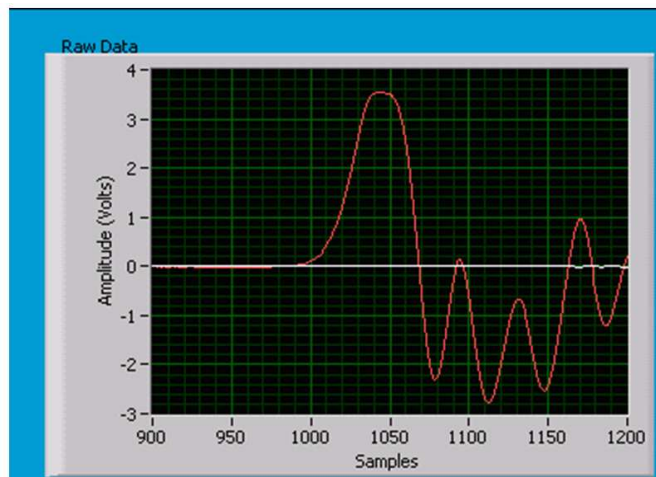


Figure 10. Hopkinson bar test to find stops. A gain of 10 was used in this test to 60000 G. The maximum output for this device was 350 mV, or the equivalent of about 40000 G. Stops are engaged.

Some testing was also performed with a Hopkinson bar and a thermal chamber, to determine thermal sensitivity shifts. The results confirmed the expected moderate negative slope of sensitivity as temperature increases. Future tests will be performed at temperatures below ambient. Due to the concentration of dopants used in the gauges, it is expected the same slope will be maintained over the entire military temperature range.

A simpler measurement over the temperature range is that of Zero Measurand Output (ZMO, also referred to as bias or offset), shown in Figure 11.

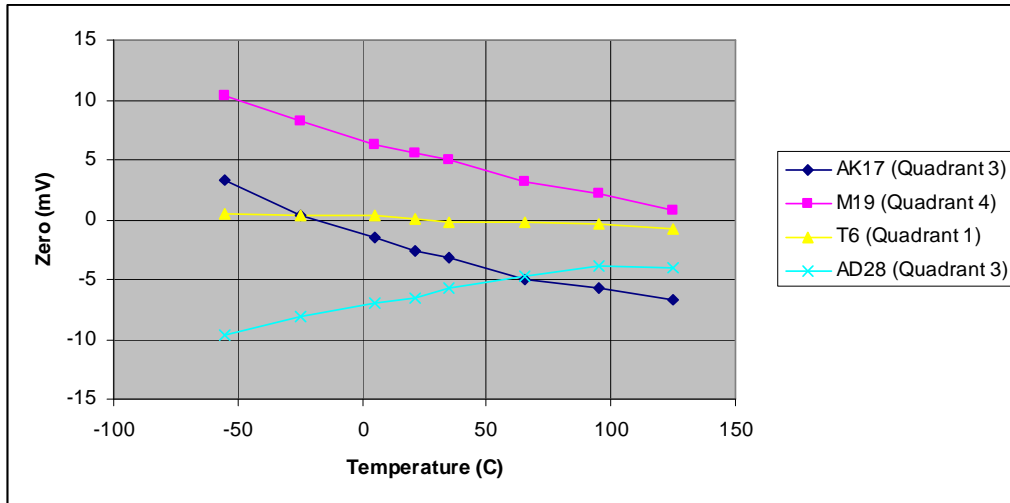


Figure 11. Thermal zero shift. The thermal shift of ZMO is plotted over the military temperature range. As shown, the thermal excursion was less than 10 mV. All values stated are with 10V excitation. (ZMO at room temperature for the total population had an average value of 2 mV, and a standard deviation of 6mV; design adjustments will create smaller values in the next round.)

Related to thermal performance, it was found that smaller excitation voltage resulted in proportionately smaller values of ZMO and thermal shifts. It was a very linear relationship with excitation voltage, as shown in Figure 12, and described below.

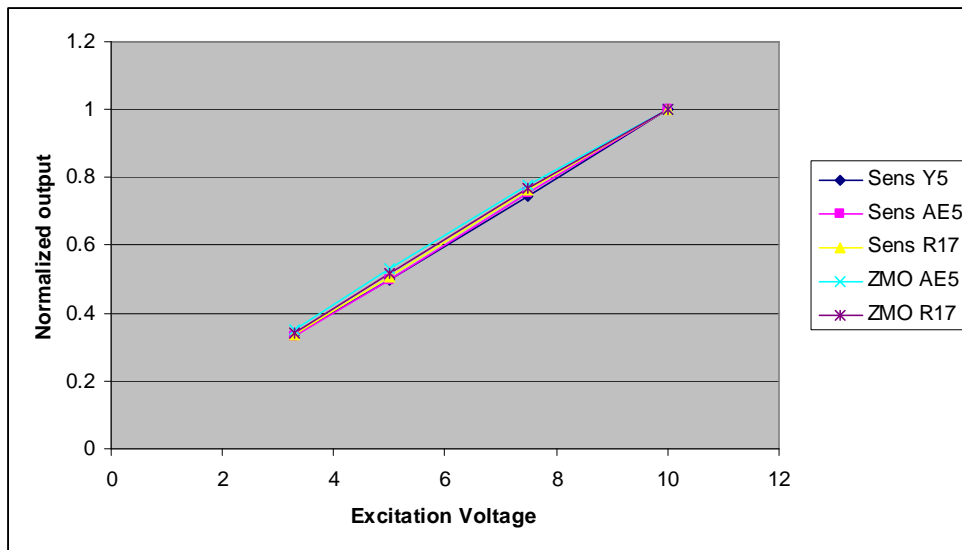


Figure 12. Effect of excitation voltage on sensitivity and ZMO. To show the linearity of the changes of sensitivity and ZMO due to excitation, the absolute values at each level were normalized by dividing by the value at 10V.

The linearity observed in zero and sensitivity are not necessarily true with the traditional sensor with its much lower bridge resistance. That sensor’s microscopic “etch-freed” gauges carry ten times the current of the new sensor, and have little heat sinking, therefore experience significant self-heating. This creates a

unique resistance and thermal profile for each excitation used. This results in nonlinearity, so values are not necessarily proportional to excitation, and are less accurately predicted.

The high resistance gauges in the new sensor have power dissipation that is an order of magnitude smaller. Since they are implanted into the heat sink of the flexures, these self-heating effects are further minimized, and the parameters of sensitivity and zero are a more linear function of excitation. Similarly, the warm-up drift is small.

Because transverse sensitivity is increasingly important in the measurement of the motion of vehicles, the new sensor was designed specifically with the symmetry that would result in low values. The following tests were performed to verify this. Although transverse sensitivity measurements are difficult to do with low sensitivity shock sensors, the improved technique shown in Figure 13 gave the results shown in Figure 15.

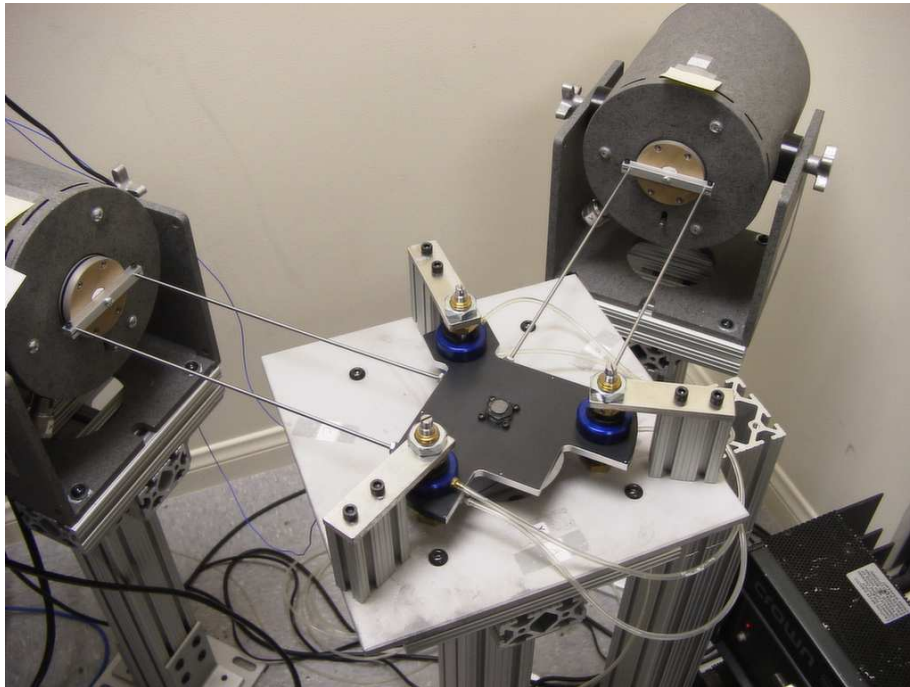


Figure 13. Transverse sensitivity testing apparatus. The equipment and technique were described in [3].

The sensors were placed with mounting surfaces on the plate shown in Figure 13, orienting sensitive axes normal to the plate. The plate was constrained to planar motion by three pairs of air bearing pads. Two shakers drove the plate in an orbit to test all directions of transverse output. The vertical motion of the plate was shown to be on the order of a micrometer, whereas the transverse motion was more than 1000 times larger, several millimeters, guaranteeing that the error of the measurement due to motion in the sensitive axis was 0.1% or less.

As depicted in Figure 14, it was known that one source of transverse sensitivity is simply the precision with which the sensor is mounted with respect to the mounting surface of the housing. The tilt of the sensor, given by angle ϕ , places a component of the sensitive axis in the mounting plane, resulting in transverse sensitivity. From the basic geometry, if the angle of tilt has a value of 0.01 radian, that angle would contribute to the transverse component of sensitivity by 1%. That angle ϕ was measured directly using the apparatus depicted in the figure.

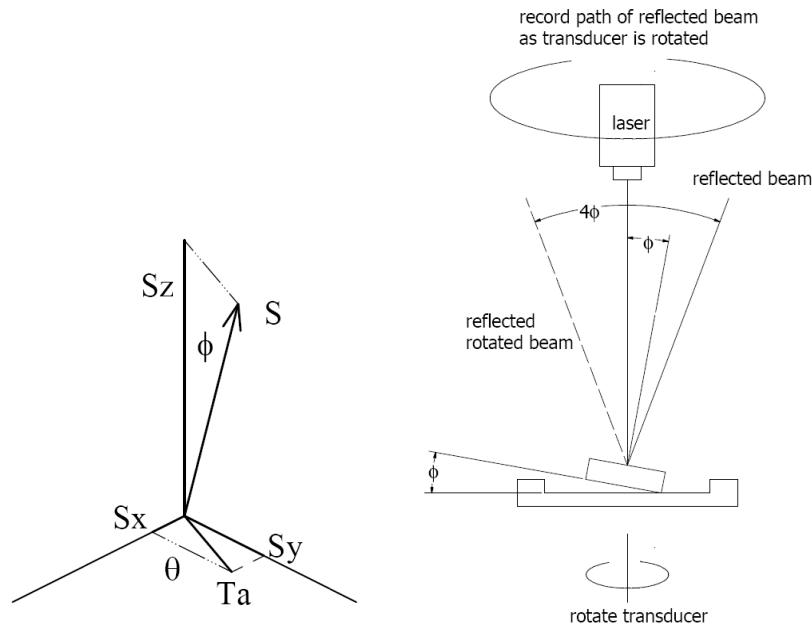


Figure 14. Transverse sensitivity as defined by a tilt, left, and determination of that tilt of sensor as mounted in a housing, right. The angle ϕ can cause a component of the overall sensitivity S to appear as absolute transverse sensitivity, T_a , in the mounting plane. The value of that tilt was determined by reflecting a laser beam off the lid of the sensor, and measuring the diameter of the path of the reflected spot when the housing was rotated.

Transverse sensitivity measurements were taken on seven sensors in titanium housings (prior to having covers welded on, so the tilt could be measured), and results were graphed in Figure 15. The line in the graph shows the values of transverse sensitivity which would be expected due to tilt alone. Another source would be inherent in the sensor itself. In a well designed sensor a transverse input results in strains of such magnitude and polarity that the outputs of the gauges cancel in the bridge. Inherent transverse sensitivity would be due to structural asymmetries in the mass and flexures, or electrical asymmetries in the piezoresistive gauges, which might result in disruption of that cancellation.

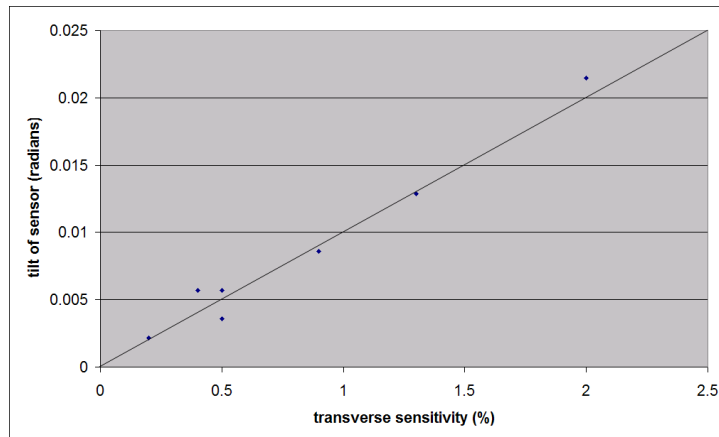


Figure 15. Transverse sensitivity vs mounting angle of the sensor. Data from sensors is plotted as points, and the line relates the transverse sensitivity which would be expected due to a given angle of tilt.

The fact that the data lies close to the line in Figure 15 implies that most of the measured sensitivity is due to tilt, and therefore the inherent transverse sensitivity might be no larger than 0.2% for this population of sensors. With moderate attention paid to the parallelism in mounting future sensors, it is possible that

overall transverse sensitivities of the finished transducer might be on the order of a few tenths of a percent, which is roughly an order of magnitude better than usual.

Conclusion

A new PR MEMS shock sensor has been developed, featuring over travel stops and damping intended to improve survivability, and high input resistance for low power consumption. Measurements confirmed dynamic and thermal performance, and the exceptional transverse sensitivity confirmed the effectiveness of the symmetry inherent in the advanced techniques used in processing.

Acknowledgments

The author wishes to acknowledge and thank Andrea Tombros and An-Shyang Chu of PCB Piezotronics for converting a theoretical design into a functional silicon sensor.

References

1. V. I. Bateman, F. A. Brown, N. T. Davie, M. A. Nusser, "High Shock, High Frequency Characteristics of a Mechanical Isolator for a Piezoresistive Accelerometer", Proceedings of the 18th Transducer Workshop, Colorado Springs, CO, June 20-22, 1995.
2. R. D. Sill, S. H. Kim, "Accelerometer Shock Sensitivity Calibration Using a Pneumatic Exciter", Proceedings of the 77th Shock and Vibration Symposium, 77th Shock and Vibration Symposium, Monterey, CA, Oct 29-Nov 3, 2006.
3. R. D. Sill, E. J. Seller, "Accelerometer Transverse Sensitivity Measurement Using Planar Orbital Motion", Proceedings of the 77th Shock and Vibration Symposium, Monterey, CA, Oct 29-Nov 3, 2006.